Excitons in 2D perovskites for ultrafast terahertz photonic devices

Kumar, Abhishek; Solanki, Ankur; Manjappa, Manukumara; Ramesh, Sankaran; Srivastava, Yogesh Kumar; Agarwal, Piyush; Sum, Tze Chien; Singh, Ranjan

2020

APPLIED PHYSICS

Excitons in 2D perovskites for ultrafast terahertz photonic devices

Abhishek Kumar[1,2]*, Ankur Solanki[1]*, Manukumara Manjappa[1,2], Sankaran Ramesh[1,3], Yogesh Kumar Srivastava[1,2], Piyush Agarwal[1,2], Tze Chien Sum[1]†, Ranjan Singh[1,2]†

In recent years, two-dimensional (2D) Ruddlesden-Popper perovskites have emerged as promising candidates for environmentally stable solar cells, highly efficient light-emitting diodes, and resistive memory devices. The remarkable existence of self-assembled quantum well (QW) structures in solution-processed 2D perovskites offers a diverse range of optoelectronic properties, which remain largely unexplored. Here, we experimentally observe ultrafast relaxation of free carriers in 20 ps due to the quantum confinement of free carriers in a self-assembled QW structures that form excitons. Furthermore, hybridizing the 2D perovskites with metamaterials on a rigid and a flexible substrate enables modulation of terahertz fields at 50-GHz modulating speed, which is the fastest for a solution-processed semiconductor-based photonic device. Hence, an exciton-based ultrafast response of 2D perovskites opens up large avenues for a wide range of scalable dynamic photonic devices with potential applications in flexible photonics, ultrafast wavefront control, and short-range wireless terahertz communications.

INTRODUCTION

In recent years, organic-inorganic hybrid three-dimensional (3D) perovskites have seen unprecedented rapid development due to their outstanding optoelectronic properties such as large diffusion lengths, excellent charge carrier mobilities, bandgap tunability, high optical gain, and nonlinear response along with low-cost fabrication techniques (1–6). However, their instability in ambient conditions hinders their large-scale applications (7, 8). In contrast, 2D Ruddlesden-Popper (RP) perovskites offer far better opportunities compared to their 3D counterparts (9, 10). Their excellent ambient stability, along with abundant tunable optoelectronic properties and high quantum efficiency, makes them ideal for a range of electronic and optical applications (11–14). In recent times, RP perovskites have shown excellent light-emitting diode (LED) performance and desirable photovoltaic efficiency (9, 15). Moreover, the existence of self-assembled quantum wells (QWs) due to the alternate arrangement of organic and inorganic atomic layers provides an additional relaxation pathway for the photo-excited free carriers to relax back at ultrafast time scales, which makes them a perfect candidate for ultrafast active photonic devices (5, 16, 17). Since the early days, there has been a huge demand for ultrafast tunable devices, especially at terahertz (THz) frequencies, as they provide tremendous opportunities for a wide range of applications ranging from imaging, spectroscopy, and wireless communication (18–22). To achieve unprecedented control over THz waves, metamaterials have been extensively used because of their tunable optical properties through structural reconfiguration (23). Furthermore, integrating metamaterials with semiconductors offer a unique platform to dynamically control and manipulate the THz waves to investigate the interface coupling effects in the resulting heterostructures (24, 25).

Recently, many developments have focused on functionalization of the metamaterials by integrating them with dynamic materials like semiconductors (24, 26–30), liquid crystals (31), superconductors (32), graphene (33), and microelectromechanical systems (34), where the intrinsic properties of these metamaterials can be modulated by introducing external stimuli such as voltage bias, optical light, and temperature. Split-ring resonators (35) are arguably the most studied meta-atoms, where, by breaking the structural symmetry, the non-radiative mode that manifests as Fano resonance can be excited (36–38). Fano resonance offers a strong-field confinement of electric fields, showing high sensitivity toward the surrounding medium, which makes it a perfect platform for light-matter interaction, sensing (39, 40), lasing spaser (41), and slow-light devices (42). Thus, a strong interaction of dynamic materials with sharp Fano resonances becomes important to investigate the role of quasi-particles such as photoexcited free carriers and excitons in realizing ultrafast control of planar photonic metadevices.

Here, we report a facile ultrafast THz photonic device by integrating 2D perovskites with the THz metamaterial for advanced manipulation of THz waves. The existence of QWs in the 2D perovskite thin film offers stable excitons at room temperature by localizing the photoexcited free carriers in QWs, which leads to ultrafast relaxation of charge carriers. Hence, the synergic relation of this material with scalable metamaterials offer an efficient active metamaterial with enhanced optical features. In this work, we explore the dynamics of free charge carriers and excitons in a pure 2D perovskite thin-film using time-resolved THz spectroscopy (TRTS) measurements. Furthermore, we demonstrate an ultrafast active metadevice using the solution-processed 2D perovskite thin film spin-coated over THz metamaterial resonators for THz applications. Here, we achieve 93% modulation of Fano resonance amplitude, showing ultrafast switching times of 20 ps (i.e., ~50-GHz modulation speed) in the 2D perovskite-based hybrid metadevice, which is extremely fast for the solution-processed semiconductor-based hybrid metadevices. Furthermore, the ease of device fabrication enables

[1]Division of Physics and Applied Physics, School of Physical and Mathematical Sciences, Nanyang Technological University, 21 Nanyang Link, Singapore 637371, Singapore. [2]Center for Disruptive Photonic Technologies, The Photonics Institute, 50 Nanyang Avenue, Nanyang Technological University, Singapore 639798, Singapore. [3]Energy Research Institute @NTU (ERI@N), Interdisciplinary Graduate School, Nanyang Technological University, 50 Nanyang Avenue, S2-B3a-01, Singapore 639798, Singapore.
*These authors contributed equally to this work.
†Corresponding author. Email: tzechien@ntu.edu.sg (T.C.S.); ranjans@ntu.edu.sg (R.S.)

the translation of the hybrid metadevice onto the flexible substrate, which opens up new avenues for many potential applications such as ultrafast flexible photonics and optoelectronics devices. In comparison to conventional active metamaterials (24–26, 29), the proposed 2D perovskite-based hybrid metadevice can also serve as the quantum many-body system to study the strong exciton-photon and photon-phonon coupling to explore the novel physics for disruptive photonic technologies.

RESULTS

Structural and optical characterization of perovskite thin films

The general formula for RP perovskite family is $(RNH_3)_2A_{n-1}M_nX_{3n+1}$, where RNH_3 is an organic cation, A is a monovalent organic cation, M is a divalent metal cation, X is a halide anion, and n represents the number of $[MX_6]^{4-}$ octahedral layers sandwiched between organic cation layers. In this study, we used simple configurations of the RP family perovskite [i.e., $n = 1$ or pure 2D perovskites; chemical formula: $(C_6H_5(CH_2)_2NH_3)_2PbI_4$ or $((PEA)_2PbI_4)$], mixed 3D-2D perovskite [i.e., $n = 2$; $((C_6H_5(CH_2)_2NH_3)_2(CH_3NH_3)PbI_7$ or $((PEA)_2MAPbI_4)$], and pure 3D perovskite (i.e., $CH_3NH_3PbI_3$) (see Materials and Methods for details). Film morphology, x-ray diffraction (XRD) pattern, and ultraviolet-visible (UV-vis) absorption spectrum for all these films were measured to confirm the good quality of the films, as presented in figs. S1 and S2. On the basis of the XRD spectra measured (fig. S2B), pure 2D perovskites are preferentially aligned in the (004) plane, while mixed 2D-3D and pure 3D perovskites are preferentially oriented in the (110) plane (43). Structurally, in the pure 2D perovskite film, the two-consecutive lead iodide octahedral layers are separated by two layers of large organic spacer cations, which are held together via weak van der Waals forces. The octahedral structure of lead halide leads to the low-energy barrier for the charge carriers, while poor conductivity of the organic spacer leads to the higher energy barrier and thus forms the QW structure. The presence of QWs provide an additional channel to localize the free carriers via exciton formation, which facilitates the ultrafast free carrier relaxation.

Figure 1A shows the normalized free carrier excitation and relaxation dynamics in 3D, mixed 3D-2D, and pure 2D perovskite films, respectively, measured using optical pump and THz probe (OPTP) measurement technique. All three perovskite films were illuminated with a 400 nm (3.1 eV) optical pump beam (which is above the energy bandgap of all three perovskites, i.e., $E_{g, 3D} = 1.5$ eV, $E_{g, 3D-2D} = 1.8$ eV, and $E_{g, 2D} = 2.2$ eV) (see fig. S2) and with a pump fluence of 750 µJ/cm². Figure 1A shows the contrasting difference in the free carrier relaxation, where the 3D perovskite exhibits slower relaxation compared to mixed 3D-2D. Swift relaxation in the 2D perovskite film occurs due to the presence of a large number of QWs, where exciton localizes inside the QW structures (Fig. 1, B and C) and provides an additional channel for the faster relaxation of free carriers. This unique feature of the 2D perovskite separates it from other solution-processed semiconductors and opens up a new avenue for ultrafast photonics. Note that the potential of the solution-processed 3D perovskite integrated with THz asymmetric split-ring resonator (TASR) structures has been previously demonstrated (44). Similar switching properties in the 3D-2D perovskite system are expected, as indicated by the relaxation dynamics. Therefore, we have further performed an in-depth investigation on the pure 2D perovskite film to use the exciton-mediated ultrafast feature of the photogenerated free carriers to control the THz field by integrating
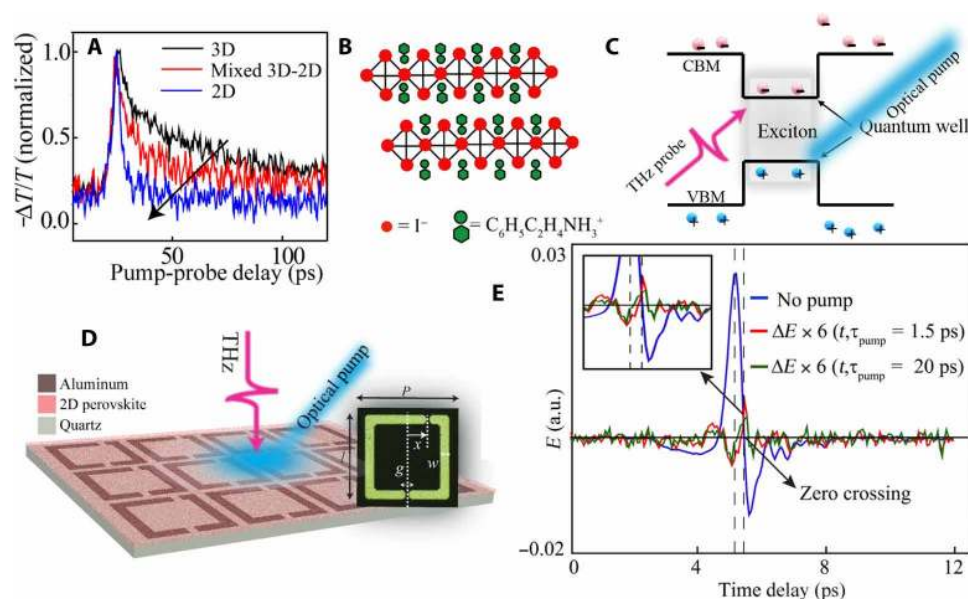
Fig. 1. Ultrafast measurement of 2D perovskite. (**A**) Free carrier excitation and relaxation dynamics of 3D perovskite (black solid curve), mixed 3D-2D perovskite (red solid curve), and pure 2D perovskite (blue solid curve) thin films. All three perovskite thin films are photoexcited using a 400-nm pump beam at 750 µJ/cm². (**B**) Schematic of the 2D perovskite crystal structure that form QWs. (**C**) Schematic of the quantum confinement of free carriers within the QW structure of the pure 2D perovskite. (**D**) Artistic illustration of the perovskite-coated hybrid metadevice, where the 2D perovskite is spin-coated (thickness 60 nm) on the top of TASR and is photoexcited using a 400-nm optical pump beam with THz as the probe. Inset shows the dimensions of the unit cell, where $l = 60$ µm, $x = 15$ µm, $w = 6$ µm, $g = 3$ µm, and square periodicity $p = 75$ µm. (**E**) Transmission of THz electric field (blue solid line) and photomodulation of the THz pulse $\Delta E(t)$ measured at $\tau_{pump} = 1.5$ ps (red solid curve) and 20 ps (green solid line) in the 2D perovskite thin film. The inset shows the THz electric field zoomed at the zero-crossing point. a.u., arbitrary units.

with TASR structures. The architecture of the 2D perovskite-based hybrid metadevice is shown in Fig. 1D. The TASRs are fabricated on the z-cut quartz substrate using a conventional photolithography technique (details are provided in Materials and Methods), where the perovskite thin film (thickness 60 nm) is spin-coated on top of the metallic resonators.

Pumping the perovskite thin film above the bandgap (2.4 eV) with an optical pump beam of wavelength 400 nm (3.1 eV) generates free carriers and excitons. We used the OPTP to unveil the dynamics of free carriers and excitons in the 2D perovskite thin film. In OPTP experiment, the attenuation in peak amplitude of THz pulse is proportional to the real part of the photoconductivity, which mostly arises due to in-phase motion of free electrons with the THz electric fields (45–48). The dynamics of THz amplitude change is recorded by varying the pump delay time scanning at the peak of the THz pulse as shown in Fig. 1E. While on the other hand, the photo-induced phase shift of the THz pulse is proportional to the imaginary part of the photoconductivity, which arises because of the out-of-phase motion of free carriers with THz electric field and the polarizability of excitons (45–48). The dynamics of the THz phase is mapped out by pump delay time scanning at the zero crossing of the THz pulse, as shown in Fig. 1E. Figure 1E demonstrates the THz electric field pulse transmitted from the unexcited perovskite thin film (blue solid curve) and photoinduced change in THz pulse $\Delta E(t)$ at different pump-probe delay times (red and green solid curves correspond to τ_{pump} of 1.5 and 20 ps, respectively). For clarity, $\Delta E(t)$ is magnified six times. The presence of excitons induces a phase shift in the THz pulse. We calculated the real and imaginary part of photoconductivity by measuring the change in THz amplitude at peak point and zero crossing of the THz pulse, which are shown in Fig. 2. Furthermore, to illustrate the effect of phase induced by the exciton, we measured the change in THz amplitude at different points on THz pulse by fixing the THz delay at different points as shown in fig. S3.

Figure 2A depicts the free carrier excitation and relaxation dynamics for different pump fluences by monitoring the change in THz amplitude (ΔT) at peak point, while Fig. 2B shows the exciton dynamics acquired by monitoring ΔT at zero crossing of the THz pulse, which mainly accounts for the phase shift. For clarity, the graphs corresponding to the various pump fluences are vertically offset. In section S2, we present the THz transient without vertical offset. Free charge carrier relaxation in the 2D perovskite thin film shows an ultrafast recombination time, where relaxation occurs within picosecond time scales (Fig. 2A). To understand the relaxation dynamics of photoexcited free carriers and excitons, we fitted THz transient dynamics at different pump fluences using biexponential decay functions $[A_1 \exp(-t/\tau_1) + A_2 \exp(-t/\tau_2)]$ (details are given in section S2), where τ_1 and τ_2 represent the time constants for the fast and slow processes, respectively. In free carrier relaxation processes, the biexponential fit reveals that the initial fast relaxation process is almost independent (~0.2 ps) of the excitation density, while the slow process becomes slower with higher excitation fluence as shown in Table 1. Because the fast relaxation time (τ_1) is independent of pump fluence, Auger- and trap-assisted relaxation processes are ruled out. This trend in the time constants reveal that the fast relaxation process (τ_1) is mainly assisted by electron-phonon scattering, as phonon-mediated relaxations are either independent of pump fluence (at medium) or increases due to hot phonon effect at high pump fluence (49, 50). Similar fluence-dependent carrier lifetime has been observed in graphene (50) and other 2D materials (47, 51). While on other hand, τ_2 is attributed as trap-assisted recombination, as it increases with pump fluence. An important point to be noted here is that the slow relaxation time (τ_2) shows the ultrafast recovery, which falls in the range of picoseconds. This ultrafast relaxation arises due to the existence of QWs where free carriers get localized due to quantum confinement and form excitons.

Following the previous studies on transition metal dichalcogenides (47, 51), to unveil the exciton dynamics in the 2D perovskite, we fitted the measured imaginary part of photoconductivity (Fig. 2B) using biexponential decay function and the fitted parameters are shown in Table 2. The fit reveals that both the decay time constants
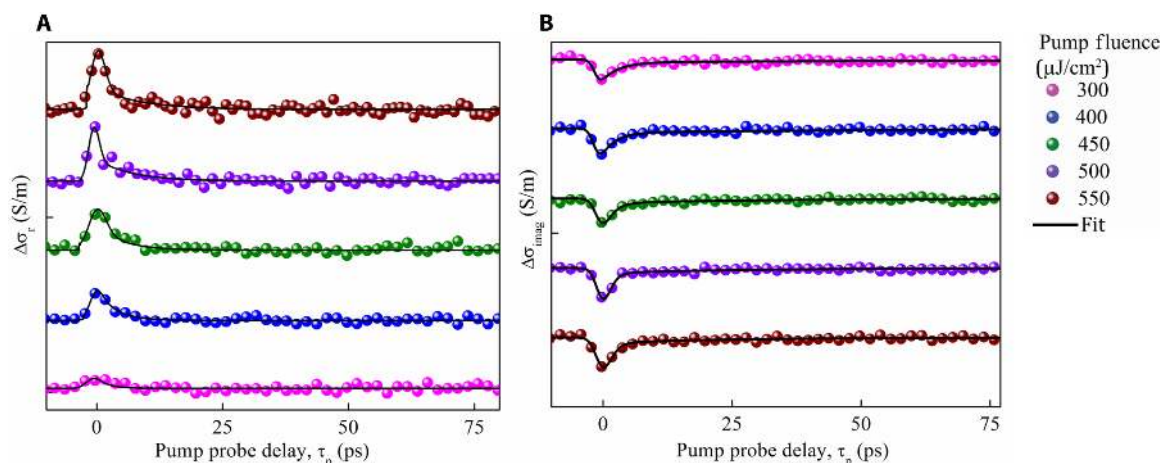

Fig. 2. Transient real and imaginary THz photoconductivity at different pump fluences. (**A**) Transient real photoconductivity at different pump fluences recorded by scanning the peak THz amplitude by varying the pump delay time in picoseconds. (**B**) Transient imaginary photoconductivity recorded by monitoring the change in THz amplitude at zero crossing. For clarity, different pump fluence data are vertically offset. Black solid line (A and B) represents the biexponential fit (details are given in section S2). The individual spectra of real and imaginary part of photoconductivity at different pump fluences are shown in fig. S4.

Table 1. Time constants of the free carrier dynamics extracted by fitting the THz transient measured (Fig. 2A) at peak position of THz pulse using biexponential decay function.

Pump fluence ($\mu J/cm^2$)	τ_1 (ps)	τ_2 (ps)
300	0.23 ± 0.04	2.9 ± 0.2
400	0.18 ± 0.01	3.5 ± 0.4
450	0.26 ± 0.01	5.0 ± 0.1
500	0.17 ± 0.01	7.2 ± 0.9
550	0.20 ± 0.01	9.0 ± 2.0

Table 2. Time constants of the exciton dynamics extracted by fitting the THz transient measured (Fig. 2B) at zero crossing of THz pulse using biexponential decay function.

Pump fluence ($\mu J/cm^2$)	τ_1 (ps)	τ_2 (ps)
300	3.2 ± 0.4	70 ± 30
400	2.5 ± 0.2	60 ± 10
450	1.6 ± 0.3	31 ± 6
500	1.2 ± 0.3	28 ± 5
550	1.1 ± 0.2	24 ± 5

(τ_1 and τ_2) decrease with pump fluence, which implies that the exciton relaxation becomes faster at larger pump fluence. We attribute this as the many-body Auger-assisted recombination, as it highly depends on carrier density and becomes faster with increase of pump fluences.

The optical characterization of the hybrid metadevice was performed using OPTP measurement scheme (see Materials and Methods). The frequency-dependent transmission spectra at various pump fluences are shown in Fig. 3A, which were calculated using normalized transmission, $T(\omega) = |\frac{E_s(\omega)}{E_r(\omega)}|$, where $E_s(\omega)$ and $E_r(\omega)$ are Fourier-transformed frequency domain electric field spectra of the sample and the substrate, respectively. In the absence of optical pump beam, the transmission spectra exhibits strong asymmetric spectral profile (black solid curve) at 0.7 THz, which is a signature of Fano resonance. Photoexciting the perovskite thin film using the femtosecond laser beam with an energy of 3.1 eV generates free photocarriers in the perovskite thin film that gradually shortens the capacitive gap in the resonators. As a result, the amplitude of Fano resonance starts to reduce with increase in pump fluence and completely switches off at 250 $\mu J/cm^2$, as shown in Fig. 3A. To emulate the experimental result, we further performed numerical simulations using a commercially available CST microwave studio software. In simulations, the structure was simulated using the periodic boundary conditions in x and y directions. Aluminum (Al) metal (thickness, 200 nm) was modeled as a lossy metal with a conductivity (σ_{dc}) of 3.57×10^7 S/m, and the dielectric constant of the quartz substrate was 4.2. The simulated THz transmission response of the hybrid metadevice for different photoconductivity values of the perovskite thin film is shown in Fig. 3B. Varying the photoconductivity in simulation is equivalent to increasing the pump fluence in the experiment. The photoconductivity values were extracted from the time resolved THz photoconductivity measurements of the bare 2D perovskite thin film for different pump fluences (see section S7).

In addition, we provide the simulated electric field distribution at the Fano resonance frequency (0.7 THz) for different photoconductivity values of the perovskite thin film and are shown in Fig. 3C. When the photoconductivity of the perovskite thin film is zero, we observe high electric field confinement in the capacitive gap (Fig. 3C). Further increasing the photoconductivity of the perovskite thin film shortens the capacitive gap, which results in pronounced suppression of Fano resonance amplitude and reduction of electric field strength in the capacitive gap (Fig. 3C).

Ultrafast switching of Fano resonances

To unveil the ultrafast feature of the 2D perovskite-based hybrid metadevice, we performed the transmission measurements at dif-ferent pump-probe delay times (τ_p), and the corresponding THz transmission spectra are shown in Fig. 4A. The photoexcitation of the perovskite thin film instantly generates the free carriers, which rapidly decay back to the steady state within 20 ps (as discussed previously). The charge carrier dynamics of the pristine 2D perovskite thin film for pump fluence (250 $\mu J/cm^2$) is shown in the inset in Fig. 4A, where various time delays (τ_p) are marked with different colored dots, and the corresponding transmission spectra are shown in Fig. 4A. The black dot represents the case when maximum photocarriers are excited. These excited photocarriers in the perovskite thin film shorten the capacitive gap of TASR and hence lead to a strong modulation of Fano resonance (black curve in Fig. 4A). The spectral feature of Fano resonance subsequently recovers as the free carriers relax back to the equilibrium state (green dot in the inset in Fig. 4A). Figure 4A exhibits the spectral evolution of Fano resonance at different τ_p, where it can be observed that the complete Fano spectral profile is retrieved within 20 ps.

To quantify the modulation at different pump fluences, we calculated the modulation depth of the Fano resonance amplitude using the relation, Modulation $(M) = \frac{|T_{Off} - T_{On}|}{T_{Off}} \times 100\%$, where T_{off} and T_{on} are the amplitude of Fano transmission without and with the influence of optical pump, respectively (shown in Fig. 4B), from the experimentally recorded transmission spectra (Fig. 3A). We observe a systematic increment in the modulation depth with pump fluences and achieve near-unity modulation ($M = 93\%$) at 250 $\mu J/cm^2$. The inset of Fig. 4B shows the contour plot of amplitude modulation of Fano resonance at different pump fluences, where the maximum modulation is achieved at 250 $\mu J/cm^2$.

Active flexible metadevice

In recent years, there has been an ever-increasing demand for flexible substrate-based technologies for designing new wearable devices, flexible cell phones, portable solar cells, and biosensors. The ease of the solution-processed 2D perovskite thin film enables the realization of an ultrafast active flexible metaphotonic device. We used the polyimide substrate due to its high flexibility, high thermal stability, and low THz absorption as the flexible platform for the devices. To maintain the simplicity, we fabricated the identical TASR array (similar to the quartz substrate) on the flexible polyimide substrate, followed by spin coating of the 2D perovskite thin film. The measurements were performed using OPTP setup, and the results are summarized in Fig. 5. The fabricated device architecture along with its flexible nature is shown in Fig. 5 (A and B), respectively. Similarly, to unveil the ultrafast feature, we further performed THz transmission
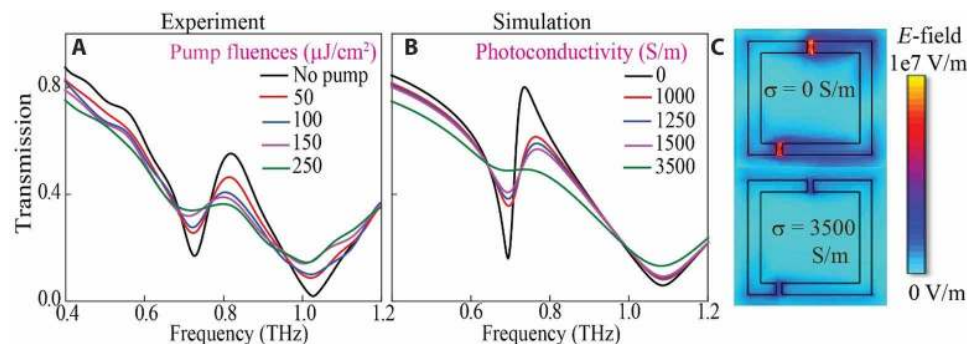
Fig. 3. Photoswitchable response of the 2D perovskite-based hybrid metadevice. (**A**) Measured amplitude transmission spectra for the metamaterial at various optical pump fluences. (**B**) Numerically simulated transmission spectra of the metamaterial coated with 2D perovskites for different photoconductivity values. (**C**) Numerically calculated *E*-field distribution for the hybrid metadevice for different photoconductivity values of the 2D perovskite thin film.
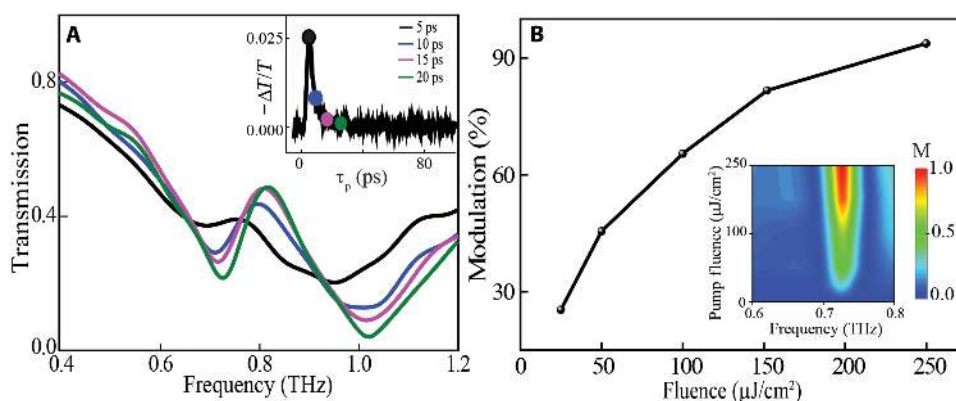

Fig. 4. Ultrafast switching of Fano resonance. (**A**) Measured transmission spectra from the 2D perovskite-coated metadevice at different pump and probe delay times. Inset shows the charge carrier relaxation in the 2D perovskite after exciting with a 400-nm pump beam at 250 μJ/cm². Black, blue, cyan, and green dots represent 10-, 14-, 20-, and 26-ps time delay between OPTP, respectively. (**B**) Amplitude modulation of Fano resonance at different optical pump fluences. The contour plot represents the amplitude modulation of the Fano resonance at different pump fluences (shown in the *y* axis).

measurements on the flexible device at different pump-probe delay times (τ_p). Figure 5C depicts the measured THz transmission spectra at different pump-probe delay times (τ_p), whereas inset shows the charge carrier dynamics in the pristine 2D perovskite thin film deposited on the flexible polyimide substrate.

Red dot represents the case when all the photogenerated free carriers are excited; hence, we observed strongly modulated Fano resonance (red curve in Fig. 5C). Subsequently, the charge carrier relaxation to equilibrium state leads to the evolution of Fano spectral feature. Here, the complete spectral feature of Fano is retrieved back within 20 ps, which confirms the ultrafast feature and is identical to the rigid (quartz) substrate results.

Furthermore, we measured Fano resonance modulation by varying the optical pump fluence. The maximum modulation of Fano resonance is observed at the pump fluence of 350 μJ/cm² (red curve in Fig. 5D), which is slightly higher compared to the quartz substrate (250 μJ/cm²). This difference in pump fluence arises due to the change in substrate (polyimide and quartz), which results in changing the morphology of perovskite thin film. The device flexibility and performance was further investigated by bending the structures to introduce the curvature in the metasurface, which is denoted by κ.

Figure 5 (E to G) shows the robustness of the flexible metadevice, where modulation of Fano resonance remains invariant irrespective of different curvatures κ_1 and κ_2.

DISCUSSION

In summary, this work unravels the exciton-mediated ultrafast free carrier relaxation in pure 2D perovskite thin films using transient THz spectroscopy. The existence of QWs in 2D perovskites facilitates the ultrafast relaxation of photoexcited free carriers via exciton formation, which aids in realizing the ultrafast THz photonic metadevice. The observed 20-ps switching time (~50-GHz modulation speed) is the fastest for a solution-processed integrated metadevice. Furthermore, the ease of integration of 2D perovskite thin film with the metamaterial fabricated on the flexible substrate opens up a new dimension in terms of applications, especially toward the realization of ultrafast flexible photonic devices. The proposed 2D perovskite-based hybrid metadevice could be an ideal platform to investigate the photon-phonon, photon-exciton, and electron-phonon coupling to explore the fundamental science and design of practical application-based devices. The integration of the 2D perovskite with metamaterials
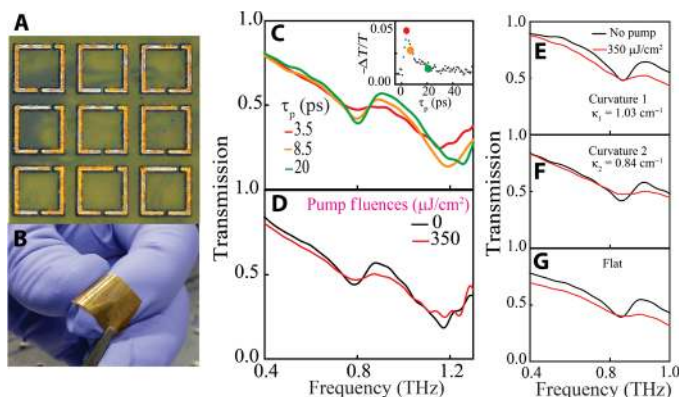
Fig. 5. Active flexible hybrid metadevice. (**A**) Optical image of the 2D perovskite-based hybrid metadevice fabricated on the polyimide flexible substrate. (**B**) Real image of the flexible metadevice showing flexibility. (**C**) Experimentally measured THz transmission through the 2D perovskite-based hybrid metadevice at different pump-probe delay times (τ_p). Inset shows the charge carrier dynamics in the pristine 2D perovskite thin film deposited on the flexible polyimide substrate. (**D**) Experimentally measured THz transmission through the metadevice at different pump fluences. (**E** to **G**) THz transmission for different curvatures of devices where curvature 1 and 2 are 1.03 and 0.84 cm^{-1} respectively. Photo credit: Manukumara Manjappa, Nanyang Technological University, Singapore.

offers many advantages in terms of device stability, low cost, and facile fabrication to push the THz applications toward large commercial scale, particularly where real-time control and manipulation of THz radiation, such as short-range wireless THz communication, ultrafast wavefront control, and photodetectors, is required.

MATERIALS AND METHODS
Device fabrication
The hybrid metadevice consists of TASR over which a thin layer of the 2D perovskite film was coated using a spin-coating technique. TASR was fabricated on both substrates (z-cut quartz substrate and polyimide flexible substrate) using standard photolithography. The detailed fabrication process is discussed below. The optical image of TASR with and without the 2D perovskite thin film is illustrated in Fig. 1 (A and B), respectively. The unit cell of TASR consists of two metallic arms, where one of the capacitive gap (g) is horizontally displaced ($x = 15$ μm) with respect to the other gap to introduce the degree of structural asymmetry (α), which is defined as $\alpha = \frac{(l_l - l_r)}{(l_l + l_r)} \times 100\%$, where l_l and l_r are the length of left and right resonator arms, respectively. The dimensions of the unit cell are depicted in the inset of Fig. 1D.

Thin-film preparation
2D [(PEA)$_2$PbI$_4$] perovskite solution was prepared by dissolving their respective precursors in N,N-dimethylformamide (DMF; Sigma-Aldrich) solvent. To obtain 2D perovskite solution, phenethylammonium iodide (PEAI) (62.2 mg/ml; C$_8$H$_{12}$IN; DyeSol) and lead (II) iodide (57.6 mg/ml; PbI$_2$; Acros Organics) were dissolved in DMF (Sigma-Aldrich) solvent. 3D perovskite solution of CH$_3$NH$_3$PbI$_3$ was prepared by dissolving 27 mg of CH$_3$NH$_3$I and 78 mg of PbI$_2$ in 1 ml of DMF solvent, while mixed 2D-3D perovskite solution was prepared by mixing 62 mg of PEAI, 20 mg of CH$_3$NH$_3$I, and 115 mg of PbI$_2$ in 1 ml of DMF. All three solutions were stirred at 70°C for 2 hours to get a clear yellow color. Thin films were prepared on the z-cut

quartz substrate and the metamaterial structure by single-step spin-coating. All perovskite films were coated at 4000 rpm for 30 s, but the 3D perovskite film was treated by toluene as the anti-solvent on the 25th second of the program to get the uniform film, while no such treatment was performed for the other two films. The 3D perovskite films were annealed at 100°C for 30 min, while the other two films were annealed at 75°C for 15 min. All these steps were performed in a N$_2$-filled glove box to prepare the different perovskite thin film. A Bruker AXS (D8 Advance) XRD equipped with Cu Kα ($\lambda = 1.5418$ Å) x-ray source was used to collect the XRD pattern. The morphology of the perovskite films was obtained using a Bruker atomic force microscope (AFM). UV-vis absorption spectra of the perovskite films were collected using a UV-vis–near-infrared spectro-photometer (Shimadzu UV-3600).

TASR fabrication procedure
TASR was fabricated using a standard photolithography technique. In the fabrication process, initially, the substrate was cleaned using acetone and isopropyl alcohol (IPA). Later, a layer of positive photoresist with a thickness of 1.5 μm was coated after drying the substrate at 100°C for 10 min on a hot plate. Furthermore, using a mask aligner, a positive mask that consists of the resonator design was aligned on the photoresist-coated substrate, which was later exposed to UV light after prebaking at 105°C. To develop the pattern, it was soaked in the developer solution. In the final step, an aluminum metal with a thickness of 200 nm was deposited using the thermal evaporation method followed by the liftoff process in acetone to remove the undesired aluminum metal.

Time-resolved THz spectroscopy (TRTS)
The TRTS measurements were performed using the OPTP setup, which includes ZnTe crystal–based THz generation-detection and an optical pump beam to photoexcite the samples. In this case, an optical laser beam with a pulse width of ~35 fs and an energy of 6 mJ/pulse centered at 800 nm with a 1-kHz repetition rate was used for the generation of THz and the photoexcitation of the samples. The beam was split into three parts, where one part was used to pump the ZnTe crystal to generate THz, the second part was used to detect the THz, and the third part was frequency-doubled (400 nm, 3.1 eV) using barium borate (BBO) crystal to excite the 2D perovskite thin film. The 400 nm wavelength optical pump beam has an energy (3.1 eV) higher than the bandgap of 2D perovskites (2.4 eV), which photoexcites the free carriers. The diameter of the optical pump beam was 5 mm, which is larger than the diameter (4 mm) of the focused THz beam to ensures the homogeneous photoexcitation. Furthermore, the time delay (τ_p) between OPTP was controlled using a translational delay stage.

SUPPLEMENTARY MATERIALS
Supplementary material for this article is available at http://advances.sciencemag.org/cgi/content/full/6/8/eaax8821/DC1

Section S1. Measurement of change in THz transmission at different THz pulse positions
Section S2. THz transient
Section S3. Transient photoluminescence
Section S4. THz transmission from the perovskite thin film
Section S5. THz transmission from bare quartz at different pump fluences
Section S6. Free carrier density excited at various pump fluences
Section S7. Photoconductivity extraction
Fig. S1. AFM images of the 2D, mixed 3D-2D, and 3D perovskites.
Fig. S2. Optical characterization of different perovskite (2D, mixed 3D-2D, and 3D) thin films.

Fig. S3. Effect of phase change induced by exciton in THz amplitude (ΔT).
Fig. S4. Free carrier and exciton dynamics in 2D perovskite.
Fig. S5. Transient photoluminescence.
Fig. S6. THz transmission through the perovskite thin film.
Fig. S7. THz transmission through the bare z-cut quartz.
Table S1. Extracted rate constant by fitting the transient photoluminescence spectra.
Table S2. Free carrier number density at different pump fluences.

REFERENCES AND NOTES

1. A. Kojima, K. Teshima, Y. Shirai, T. Miyasaka, Organometal halide perovskites as visible-light sensitizers for photovoltaic cells. *J. Am. Chem. Soc.* **131**, 6050–6051 (2009).
2. J.-H. Im, C.-R. Lee, J.-W. Lee, S.-W. Park, N.-G. Park, 6.5% efficient perovskite quantum-dot-sensitized solar cell. *Nanoscale* **3**, 4088–4093 (2011).
3. M. M. Lee, J. Teuscher, T. Miyasaka, T. N. Murakami, H. J. Snaith, Efficient hybrid solar cells based on meso-superstructured organometal halide perovskites. *Science* **338**, 643–647 (2012).
4. M. Liu, M. B. Johnston, H. J. Snaith, Efficient planar heterojunction perovskite solar cells by vapour deposition. *Nature* **501**, 395–398 (2013).
5. L. M. Herz, Charge-carrier dynamics in organic-inorganic metal halide perovskites. *Annu. Rev. Phys. Chem.* **67**, 65–89 (2016).
6. A. Solanki, P. Yadav, S. H. Turren-Cruz, S. S. Lim, M. Saliba, T. C. Sum, Cation influence on carrier dynamics in perovskite solar cells. *Nano Energy* **58**, 604–611 (2019).
7. Y. Rong, L. Liu, A. Mei, X. Li, H. Han, Beyond efficiency: The challenge of stability in mesoscopic perovskite solar cells. *Adv. Energy Mater.* **5**, 1501066 (2015).
8. Z. Wang, Z. Shi, T. Li, Y. Chen, W. Huang, Stability of perovskite solar cells: A prospective on the substitution of the a cation and X anion. *Angew. Chem. Int. Ed.* **56**, 1190–1212 (2017).
9. H. Tsai, W. Nie, J.-C. Blancon, C. C. Stoumpos, R. Asadpour, B. Harutyunyan, A. J. Neukirch, R. Verduzco, J. J. Crochet, S. Tretiak, L. Pedesseau, J. Even, M. A. Alam, G. Gupta, J. Lou, P. M. Ajayan, M. J. Bedzyk, M. G. Kanatzidis, A. D. Mohite, High-efficiency two-dimensional Ruddlesden–Popper perovskite solar cells. *Nature* **536**, 312–316 (2016).
10. Y. Chen, Y. Sun, J. Peng, J. Tang, K. Zheng, Z. Liang, 2D Ruddlesden–Popper perovskites for optoelectronics. *Adv. Mater.* **30**, 1703487 (2018).
11. M. Yuan, L. N. Quan, R. Comin, G. Walters, R. Sabatini, O. Voznyy, S. Hoogland, Y. Zhao, E. M. Beauregard, P. Kanjanaboos, Z. Lu, D. H. Kim, E. H. Sargent, Perovskite energy funnels for efficient light-emitting diodes. *Nat. Nanotechnol.* **11**, 872–877 (2016).
12. D. H. Cao, C. C. Stoumpos, O. K. Farha, J. T. Hupp, M. G. Kanatzidis, 2D homologous perovskites as light-absorbing materials for solar cell applications. *J. Am. Chem. Soc.* **137**, 7843–7850 (2015).
13. L. Pedesseau, D. Sapori, B. Traore, R. Robles, H.-H. Fang, M. A. Loi, H. Tsai, W. Nie, J.-C. Blancon, A. Neukirch, S. Tretiak, A. D. Mohite, C. Katan, J. Even, M. Kepenekian, Advances and promises of layered halide hybrid perovskite semiconductors. *ACS Nano* **10**, 9776–9786 (2016).
14. I. C. Smith, E. T. Hoke, D. Solis-Ibarra, M. D. McGehee, H. I. Karunadasa, A layered hybrid perovskite solar-cell absorber with enhanced moisture stability. *Angew. Chem. Int. Ed.* **53**, 11232–11235 (2014).
15. X. Yang, X. Zhang, J. Deng, Z. Chu, Q. Jiang, J. Meng, P. Wang, L. Zhang, Z. Yin, J. You, Efficient green light-emitting diodes based on quasi-two-dimensional composition and phase engineered perovskite with surface passivation. *Nat. Commun.* **9**, 570 (2018).
16. R. L. Milot, R. J. Sutton, G. E. Eperon, A. A. Haghighirad, J. Martinez Hardigree, L. Miranda, H. J. Snaith, M. B. Johnston, L. M. Herz, Charge-carrier dynamics in 2D hybrid metal–halide perovskites. *Nano Lett.* **16**, 7001–7007 (2016).
17. G. Xing, B. Wu, X. Wu, M. Li, B. Du, Q. Wei, J. Guo, E. K. L. Yeow, T. C. Sum, W. Huang, Transcending the slow bimolecular recombination in lead-halide perovskites for electroluminescence. *Nat. Commun.* **8**, 14558 (2017).
18. A. Y. Pawar, D. D. Sonawane, K. B. Erande, D. V. Derle, Terahertz technology and its applications. *Drug Invent. Today* **5**, 157–163 (2013).
19. M. Tonouchi, Cutting-edge terahertz technology. *Nat. Photonics* **1**, 97–105 (2007).
20. Q. Wu, T. D. Hewitt, X.-C. Zhang, Two-dimensional electro-optic imaging of THz beams. *Appl. Phys. Lett.* **69**, 1026–1028 (1996).
21. S. M. Kim, F. Hatami, J. S. Harris, A. W. Kurian, J. Ford, D. King, G. Scalari, M. Giovannini, N. Hoyler, J. Faist, G. Harris, Biomedical terahertz imaging with a quantum cascade laser. *Appl. Phys. Lett.* **88**, 153903 (2006).
22. T. Yasuda, T. Yasui, T. Araki, E. Abraham, Real-time two-dimensional terahertz tomography of moving objects. *Opt. Commun.* **267**, 128–136 (2006).
23. D. R. Smith, J. B. Pendry, M. C. K. Wiltshire, Metamaterials and negative refractive index. *Science* **305**, 788–792 (2004).
24. H.-T. Chen, W. J. Padilla, J. M. O. Zide, A. C. Gossard, A. J. Taylor, R. D. Averitt, Active terahertz metamaterial devices. *Nature* **444**, 597–600 (2006).
25. W. J. Padilla, A. J. Taylor, C. Highstrete, M. Lee, R. D. Averitt, Dynamical electric and magnetic metamaterial response at terahertz frequencies. *Phys. Rev. Lett.* **96**, 107401 (2006).
26. M. Manjappa, Y. K. Srivastava, L. Cong, I. Al-Naib, R. Singh, Active photoswitching of sharp Fano resonances in THz metadevices. *Adv. Mater.* **29**, 1603355 (2017).
27. H. Tao, A. C. Strikwerda, K. Fan, W. J. Padilla, X. Zhang, R. D. Averitt, Reconfigurable terahertz metamaterials. *Phys. Rev. Lett.* **103**, 147401 (2009).
28. K. Fan, A. C. Strikwerda, X. Zhang, R. D. Averitt, Three-dimensional broadband tunable terahertz metamaterials. *Phys. Rev. B* **87**, 161104(R) (2013).
29. H.-T. Chen, J. F. O'Hara, A. K. Azad, A. J. Taylor, R. D. Averitt, D. B. Shrekenhamer, W. J. Padilla, Experimental demonstration of frequency-agile terahertz metamaterials. *Nat. Photonics* **2**, 295–298 (2008).
30. M. R. Shcherbakov, S. Liu, V. V. Zubyuk, A. Vaskin, P. P. Vabishchevich, G. Keeler, T. Pertsch, T. V. Dolgova, I. Staude, I. Brener, A. A. Fedyanin, Ultrafast all-optical tuning of direct-gap semiconductor metasurfaces. *Nat. Commun.* **8**, 17 (2017).
31. A. Minovich, J. Farnell, D. N. Neshev, I. McKerracher, F. Karouta, J. Tian, D. A. Powell, I. V. Shadrivov, H. Hoe Tan, C. Jagadish, Y. S. Kivshar, Liquid crystal based nonlinear fishnet metamaterials. *Appl. Phys. Lett.* **100**, 121113 (2012).
32. Y. K. Srivastava, M. Manjappa, L. Cong, H. N. S. Krishnamoorthy, V. Savinov, P. Pitchappa, R. Singh, A superconducting dual-channel photonic switch. *Adv. Mater.* **30**, 1801257 (2018).
33. S. H. Mousavi, I. Kholmanov, K. B. Alici, D. Purtseladze, N. Arju, K. Tatar, D. Y. Fozdar, J. W. Suk, Y. Hao, A. B. Khanikaev, R. S. Ruoff, G. Shvets, Inductive tuning of Fano-resonant metasurfaces using plasmonic response of graphene in the mid-infrared. *Nano Lett.* **13**, 1111–1117 (2013).
34. P. Pitchappa, M. Manjappa, C. P. Ho, R. Singh, N. Singh, C. Lee, Active control of electromagnetically induced transparency analog in terahertz MEMS metamaterial. *Adv. Opt. Mater.* **4**, 541–547 (2016).
35. D. Schurig, J. J. Mock, D. R. Smith, Electric-field-coupled resonators for negative permittivity metamaterials. *Appl. Phys. Lett.* **88**, 041109 (2006).
36. B. Luk'yanchuk, N. I. Zheludev, S. A. Maier, N. J. Halas, P. Nordlander, H. Giessen, C. T. Chong, The Fano resonance in plasmonic nanostructures and metamaterials. *Nat. Mater.* **9**, 707–715 (2010).
37. R. Singh, I. A. I. Al-Naib, M. Koch, W. Zhang, Sharp Fano resonances in THz metamaterials. *Opt. Express* **19**, 6312–6319 (2011).
38. R. Singh, I. Al-Naib, W. Cao, C. Rockstuhl, M. Koch, W. Zhang, The Fano resonance in symmetry broken terahertz metamaterials. *IEEE Trans. Terahertz Sci. Technol.* **3**, 820–826 (2013).
39. A. A. Yanik, A. E. Cetin, M. Huang, A. Artar, S. H. Mousavi, A. Khanikaev, J. H. Connor, G. Shvets, H. Altug, Seeing protein monolayers with naked eye through plasmonic Fano resonances. *Proc. Natl. Acad. Sci. U.S.A.* **108**, 11784–11789 (2011).
40. C. Wu, A. B. Khanikaev, R. Adato, N. Arju, A. A. Yanik, H. Altug, G. Shvets, Fano-resonant asymmetric metamaterials for ultrasensitive spectroscopy and identification of molecular monolayers. *Nat. Mater.* **11**, 69–75 (2011).
41. N. I. Zheludev, S. L. Prosvirnin, N. Papasimakis, V. A. Fedotov, Lasing spaser. *Nat. Photonics* **2**, 351–354 (2008).
42. N. Papasimakis, N. I. Zheludev, Metamaterial-induced transparency: Sharp Fano resonances and slow light. *Opt. Photonics News* **20**, 22–27 (2009).
43. Q. Zhang, A. Solanki, K. Parida, D. Giovanni, M. Li, T. L. C. Jansen, M. S. Pshenichnikov, T. C. Sum, Tunable ferroelectricity in Ruddlesden–Popper halide perovskites. *ACS Appl. Mater. Interfaces* **11**, 13523–13532 (2019).
44. M. Manjappa, Y. K. Srivastava, A. Solanki, A. Kumar, T. C. Sum, R. Singh, Hybrid lead halide perovskites for ultrasensitive photoactive switching in terahertz metamaterial devices. *Adv. Mater.* **29**, 1605881 (2017).
45. S. A. Jensen, R. Ulbricht, A. Narita, X. Feng, K. Müllen, T. Hertel, D. Turchinovich, M. Bonn, Ultrafast photoconductivity of graphene nanoribbons and carbon nanotubes. *Nano Lett.* **13**, 5925–5930 (2013).
46. F. Wang, J. Shan, M. A. Islam, I. P. Herman, M. Bonn, T. F. Heinz, Exciton polarizability in semiconductor nanocrystals. *Nat. Mater.* **5**, 861–864 (2006).
47. C. He, L. Zhu, Q. Zhao, Y. Huang, Z. Yao, W. Du, Y. He, S. Zhang, X. Xu, Competition between free carriers and excitons mediated by defects observed in layered WSe$_2$ crystal with time-resolved terahertz spectroscopy. *Adv. Opt. Mater.* **6**, 1800290 (2018).
48. R. Ulbricht, E. Hendry, J. Shan, T. F. Heinz, M. Bonn, Carrier dynamics in semiconductors studied with time-resolved terahertz spectroscopy. *Rev. Mod. Phys.* **83**, 543–586 (2011).
49. Z. Nie, R. Long, L. Sun, C.-C. Huang, J. Zhang, Q. Xiong, D. W. Hewak, Z. Shen, O. V. Prezhdo, Z.-H. Loh, Ultrafast carrier thermalization and cooling dynamics in few-layer MoS$_2$. *ACS Nano* **8**, 10931–10940 (2014).
50. B. Gao, G. Hartland, T. Fang, M. Kelly, D. Jena, H. Xing, L. Huang, Studies of intrinsic hot phonon dynamics in suspended graphene by transient absorption microscopy. *Nano Lett.* **11**, 3184–3189 (2011).
51. X. Xing, L. Zhao, Z. Zhang, X. Liu, K. Zhang, Y. Yu, X. Lin, H. Y. Chen, J. Q. Chen, Z. Jin, J. Xu, G.-h. Ma, Role of photoinduced exciton in the transient terahertz conductivity of few-layer WS$_2$ laminate. *J. Phys. Chem. C* **121**, 20451–20457 (2017).

Citation: A. Kumar, A. Solanki, M. Manjappa, S. Ramesh, Y. K. Srivastava, P. Agarwal, T. C. Sum, R. Singh, Excitons in 2D perovskites for ultrafast terahertz photonic devices. *Sci. Adv.* **6**, eaax8821 (2020).

Science Advances

Excitons in 2D perovskites for ultrafast terahertz photonic devices

Abhishek Kumar, Ankur Solanki, Manukumara Manjappa, Sankaran Ramesh, Yogesh Kumar Srivastava, Piyush Agarwal, Tze Chien Sum and Ranjan Singh

ARTICLE TOOLS	http://advances.sciencemag.org/content/6/8/eaax8821
SUPPLEMENTARY MATERIALS	http://advances.sciencemag.org/content/suppl/2020/02/14/6.8.eaax8821.DC1
REFERENCES	This article cites 51 articles, 3 of which you can access for free http://advances.sciencemag.org/content/6/8/eaax8821#BIBL
PERMISSIONS	http://www.sciencemag.org/help/reprints-and-permissions

Use of this article is subject to the Terms of Service